Kosuke Murano, Issei Watanabe, Akifumi Kasamatsu, Safumi Suzuki, Masahiro Asada, Withawat Withayachumnankul, Toshiyuki Tanaka, and Yasuaki Monnai
Low-profile terahertz radar based on broadband leaky-wave beam steering
IEEE Transactions on Terahertz Science and Technology, 2017; 7(1):60-69

Published version at: http://doi.org/10.1109/TTHZ.2016.2624514

Low-Profile Terahertz Radar Based on Broadband Leaky-Wave Beam Steering

Kosuke Murano, Issei Watanabe, Akifumi Kasamatsu, Safumi Suzuki, Masahiro Asada, *Fellow, IEEE,* Withawat Withayachumnankul, *Senior Member, IEEE,* Toshiyuki Tanaka, and Yasuaki Monnai

***Abstract*—We demonstrate short-range terahertz radar based on a leaky-wave antenna with beam steering capability. As a proof of concept, we develop a microstrip-based periodic leaky-wave antenna driven by a vector network analyzer. By sweeping the frequency from 235 to 325 GHz, beam steering from -23° to $+15^\circ$ across the broadside can be achieved with a nearly constant beam width of 4°. Small target detection is demonstrated by locating a metal cylinder with a diameter of 12 mm placed 46 – 86 mm in front of the antenna with a mean error of 2.4 mm. The use of a leaky-wave antenna can pave a way for developing a low-loss, low-profile, and wide aperture terahertz radar. Importantly, it can be integrated with a solid-state source and a detector. The proposed approach is particularly promising for use with emerging small devices such as drones or wearable devices, where millimeter-wave radar is not suitable in terms of the resolution and system footprint.**

***Index Terms*—Terahertz radar, leaky-wave antennas, beam steering, broadside radiation, waveguide-to-microstrip couplers**

I. INTRODUCTION

HIGH spatial resolution and penetrability into non-metallic materials are the advantages of sensing with terahertz waves. While a number of studies have exploited these features in the context of imaging, the implementation of terahertz radar that enables stand-off detection with valuable range information has been underexplored both in terms of hardware and practical applications. Owing to the shorter wavelengths, terahertz radar is superior to microwave and millimeter-wave radar in terms of minimum detectable target size and the radiation aperture size. Although terahertz waves are significantly attenuated by the atmosphere, the absorption at an atmospheric window around 300 GHz is below 4 dB/km [1], which is low enough to deliver signals up to several tens of meters. So far, there exist several pioneering demonstrations of terahertz radar aiming at security applications [2]–[7]. Those proof-of-concept systems, however, remain bulky due to the use of quasi-optical components for beamforming and steering.

K. Murano, T. Tanaka, and Y. Monnai are with the Department of Applied Physics and Physico-Informatics, Keio University, Yokohama, Kanagawa, 223-8656 Japan e-mail: monnai@appi.keio.ac.jp

I. Watanabe and A. Kasamatsu are with the National Institute of Information and Communications Technology

S. Suzuki is with the Graduate School of Science and Engineering, Tokyo Institute of Technology, Tokyo 152-8552, Japan

M. Asada is with the Interdisciplinary Graduate School of Science and Engineering, Tokyo Institute of Technology, Tokyo 152-8552, Japan

W. Withayachumnankul is with the School of Electrical & Electronic Engineering, the University of Adelaide, Adelaide, SA 5005, Australia.

Manuscript received July XX, 2016; revised October XX, 2016.

In this article, we propose and experimentally demonstrate the use of a leaky-wave antenna (LWA) for implementing low-profile terahertz radar. A LWA can generate a directional beam by coherently leaking a traveling wave from a waveguide into free-space. While LWAs have been used in the microwave regime for decades [8]–[10], the application to the terahertz frequencies has recently been highlighted [11]–[18] in relation to a large radiation aperture and low-profile. Furthermore, LWAs possess another important capability of dynamic beam steering enabled by frequency sweeping [14]. In particular, periodically modulated LWAs can steer a beam from backward to forward direction across the broadside [19]–[22]. This capability is particularly relevant in the terahertz regime, where the wavefront engineering based on phase shifters is challenging.

For an experimental demonstration of the LWA-based terahertz radar, we develop a microstrip-based periodic LWA as illustrated in Fig. 1(a). Using this LWA, we can estimate the location of a small target placed in front of the LWA from the reflection coefficient available from a vector network analyzer (VNA). Although the LWA in this work is driven by a VNA as a proof-of-concept, the VNA can be replaced with rapidly evolving solid-state sources and detectors such as resonant tunneling diodes or quantum cascade lasers [23]–[26]. Such an integrated platform will allow us to implement compact terahertz radar systems for novel applications such as flight support of tiny drones [27] or human gesture recognition on wearable devices [28]. These applications require high-resolution and high-speed stand-off detection with a small system footprint. It is worth mentioning here that ultrasonic waves have comparable wavelengths, e.g. 1 mm at 340 kHz, and could be used for similar detection applications with a comparable spatial resolution. Nevertheless, the atmospheric absorption of ultrasound is very severe and reaches as high as 20 dB/m at 340 kHz [29]. As such high-frequency ultrasound cannot substitute terahertz waves for free-space detection.

This article is organized as follows. Section II explains the principle of LWA-based radar, including the range and angular resolutions. Then the LWA and coupler designs and experimental characterizations are expounded in Section III. Using this LWA, we demonstrate proof-of-concept of the radar in Section IV, and conclude the discussion in Section V.

II. PRINCIPLE OF TERAHERTZ RADAR BASED ON LEAKY-WAVE ANTENNAS

The system setup for radar demonstration is illustrated in Fig. 1(a). We implement a microstrip periodic LWA that is fed

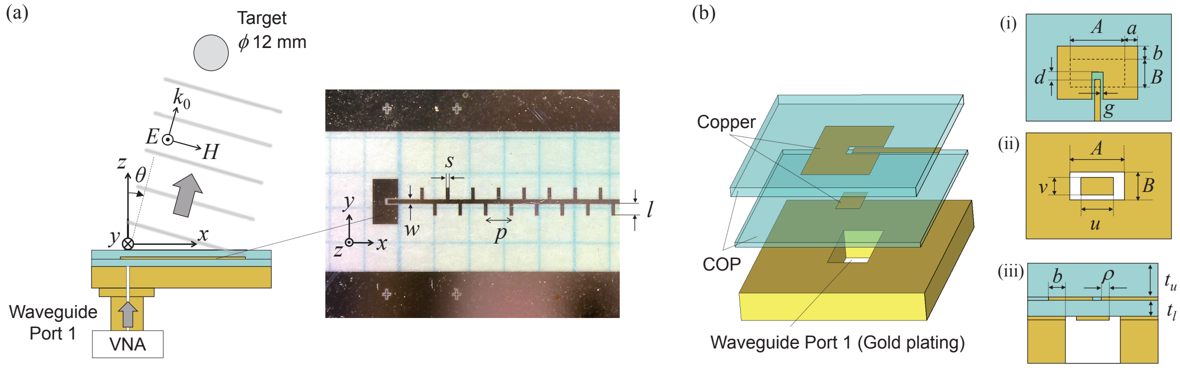

Fig. 1. (a) Illustration of the microstrip periodic LWA for terahertz radar. p=730 μm, s=100 μm, l=335 μm, w=130 μm. (b) Waveguide-to-microstrip coupler that interfaces the LWA with VNA. The copper layer is on the back side of each COP film. u=440 μm, v=260 μm, A=864 μm, B=432 μm, a=215 μm, b=155 μm, ρ=68 μm, d=70 μm, g=28 μm, t_l=50 μm, t_u=100 μm.

with a VNA. Since the VNA port is available in the form of a rectangular waveguide, the LWA-VNA interface requires a via-less planar coupler as illustrated in Fig. 1(b), which allows mode conversion between TE_{10} and quasi-TEM modes [30]. By monitoring the S-parameter of the LWA, we can determine the location of a target placed in front of the LWA. In this section, we formulate this detection procedure. The scope of our current study is limited to 2D mapping as we use a 1D LWA which generates a collimated beam only in the H-plane while diverging in the transversal E-plane.

A. Periodic Leaky-Wave Antenna

In a microstrip periodic LWA shown in Fig. 1(a), the periodic stubs collectively radiate a portion of the wave guided along the microstrip line into free-space. Along the waveguide axis, the phase profile of the radiated wave is linear and thus defines a tilted wavefront. The beam direction is governed by the following grating equation [8]

$$k_0 \sin\theta_n = \beta_g + \frac{2\pi n}{p}\,, \tag{1}$$

where k_0 is the wavenumber of free-space radiation, β_g is the propagation constant of a waveguide, p is the stub period, and θ_n is the beam angle of the n-th order diffraction measured from the broadside. As k_0 and β_g are dependent on the angular frequency ω, the angle θ_n can be varied by sweeping ω. When the LWA is sufficiently long and only $n = -1$ is allowed, the H-plane radiation pattern is approximately given by the following equation [8]

$$D(\theta,\omega) \propto \frac{\cos^2\theta}{(\sin\theta - \sin\theta_{-1})^2 + (\alpha c/\omega)^2}\,, \tag{2}$$

where θ_{-1} is given by (1) and c is the speed of light in vacuum. The factor α is an attenuation coefficient of the waveguide comprising material and radiation losses, α_m and α_r, respectively, as

$$\alpha = \alpha_m + \alpha_r. \tag{3}$$

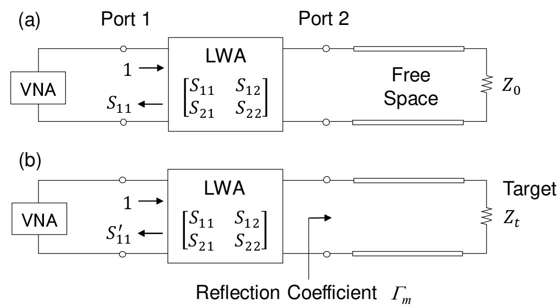

Fig. 2. Equivalent circuit representation of the radar system. (a) When there is no target, the circuit is terminated by a matched impedance Z_0. (b) When a target exists, it is modeled as a load Z_t that involves a reflection.

The radiation pattern (2) possesses its peak at $\theta = \theta_{-1}$. The 3dB width of the peak, θ_w, can be expressed as

$$\theta_w = \frac{2\alpha c}{\omega\cos\theta_{-1}}. \tag{4}$$

B. Object Detection

By considering the LWA as a two-port device, where the port 1 couples to a VNA and port 2 to free-space, we can model the radar system using an equivalent circuit approach as illustrated in Fig. 2. The location of a target can be identified by comparing the complex reflection coefficients of the LWA, $S'_{11}(\omega)$ and $S_{11}(\omega)$, with and without the target, respectively. Our goal here is to extract the range and direction of the target, (R_t, θ_t) described in the polar coordinate, from these coefficients. In this model, the presence of the target modulates the reflection coefficient, which can be described as a perturbation to S_{11} as [31]

$$\Delta S_{11}(\omega) \equiv S'_{11}(\omega) - S_{11}(\omega) = \frac{S_{12}(\omega)S_{21}(\omega)\Gamma_m(\omega)}{1 - S_{22}(\omega)\Gamma_m(\omega)}\,, \tag{5}$$

where $\Gamma_m(\omega)$ is the reflection coefficient seen towards the target from port 2 of the antenna. Assuming $S_{21}(\omega) = S_{12}(\omega) \simeq e^{-j\varphi}$ where φ expresses a phase change imposed by the LWA and $|S_{22}(\omega)\Delta S_{11}(\omega)| \ll 1$, we can derive

$$\Gamma_m(\omega) \simeq e^{j2\varphi}\Delta S_{11}(\omega). \tag{6}$$

Meanwhile, we can consider a theoretical model of the reflection coefficient based on a radar equation [8] as

$$\Gamma_a(\omega) = e^{-j\left(\frac{\omega}{c}2R_t+\phi\right)}\sqrt{\frac{G^2\left(\theta_t,\omega\right)\left(2\pi c/\omega\right)^2\sigma(\theta_t)}{\left(4\pi\right)^3 R_t^4}}\ , \quad (7)$$

where $G\left(\theta,\omega\right) \propto D\left(\theta,\omega\right)$ is the gain of the LWA, $\sigma(\theta)$ is the radar cross section of the target, ϕ is a reflection phase response of the target, and R_t is the range between the antenna and the target.

First we consider the extraction of the direction θ_t. Owing to the frequency-to-angle mapping of a LWA governed by (1), we can readout θ_t from the frequency ω_t at which the strongest reflection is observed.

$$\omega_t = \underset{\omega}{\operatorname{argmax}}\left|\Gamma_a(\omega)\right|. \quad (8)$$

In practice, we use experimentally obtained $\Gamma_m(\omega)$ instead of $\Gamma_a(\omega)$. With this ω_t, the direction θ_t is determined from (1) as

$$\theta_t = \sin^{-1}\left[\frac{\beta_g(\omega_t) - 2\pi/p}{k_0(\omega_t)}\right]. \quad (9)$$

We next consider the extraction of the range R_t. As seen in (7), $\Gamma_a(\omega)$ is a sinusoidal function of ω with a period of $2R_t/c$ in the frequency domain. This rate is equivalent to the time-of-flight (TOF) in the time domain. Therefore, an inverse Fourier transform of (7) readily identifies R_t as

$$R_t = \frac{c}{2}\underset{\tau}{\operatorname{argmax}}\left|\mathcal{F}^{-1}\left[\Gamma_m(\omega)\right]\right|\ , \quad (10)$$

where $\mathcal{F}^{-1}\left[\Gamma_m(\omega)\right]$ indicates the inverse Fourier transform of $\Gamma_m(\omega)$, and τ expresses its argument in the time domain. Note that we need to compensate for φ in (6) by shifting the temporal sequences. Also, the phase shift ϕ becomes π when the target is metal and involves a range ambiguity of half a wavelength.

C. Uncertainty Principle

We discuss the precision trade-off between the direction θ_t and the range R_t. As the LWA forms and steers a sharp beam by sweeping the frequency, a target placed sufficiently far away from the LWA receives only a narrow-band signal. The reflection coefficient $\Gamma_m(\omega)$ thus possesses a sharp peak in the frequency domain. While it helps identifying θ_t precisely, the precision of the range R_t determined by the inverse Fourier transform (10) is limited due to the uncertainty principle. Suppose $\Gamma_m(\omega)$ is sampled in the frequency domain at an interval of Δf over N points, then its discrete inverse Fourier transform has a resolution of $\Delta t = 1/(N\Delta f)$ in the time domain. The uncertainty principle for a discrete signal [32] is described in terms of the number of non-zero elements of the frequency and time sequences, N_f and N_τ, respectively, as

$$N_f \cdot N_\tau \geq N. \quad (11)$$

The lower bound of the uncertainty of the TOF is then given as $N_\tau\Delta t \geq 1/N_f\Delta f$, which is translated to the range uncertainty ΔR as

$$\Delta R \geq \frac{c}{2N_f\Delta f}. \quad (12)$$

Meanwhile, considering that the beam direction varies as a function of the frequency as in (1), the uncertainty $\Delta\theta$ around θ_t is directly related to that of the frequency, $N_f\Delta f$, as

$$\Delta\theta = \left.\frac{\partial\theta_{-1}}{\partial f}\right|_{\theta_{-1}=\theta_t} N_f\Delta f. \quad (13)$$

By combining (12) and (13), we obtain the uncertainty principle for the LWA radar as follows.

$$\Delta\theta\cdot\Delta R \geq \frac{c}{2}\left.\frac{\partial\theta_{-1}}{\partial f}\right|_{\theta_{-1}=\theta_t}. \quad (14)$$

It is noteworthy that ΔR and $\Delta\theta$ defined by the non-zero elements of the frequency and time sequences correspond to the most conservative estimation of a target location. Rather, the uncertainty is in practice associated with the apparent size of the target seen from the LWA. When the apparent size is large, $\Delta\theta$ becomes large and thus ΔR can be small. As the beam width is finite, the lower bound of $\Delta\theta$ to be considered in (14) is given by θ_w in (4).

D. Maximum Measurable Range

We consider the maximum measurable range of the radar. From (7), we can derive the physical maximum range R_p as

$$R_p = \left(\frac{G^2\left(\omega,\theta_t\right)\left(2\pi c/\omega\right)^2\sigma(\theta_t)}{(4\pi)^3\left|\Gamma_{\min}\left(\omega\right)\right|^2}\right)^{1/4}\ , \quad (15)$$

where $\Gamma_{\min}\left(\omega\right)$ represents the minimum detectable reflection coefficient, which depends on the dynamic range of the transceiver. Apart from this noise-related limit, the sampling interval also limits the maximum measurable range. When the complex S_{11} is sampled in the frequency domain at an interval of Δf, then the longest TOF that can be determined by the inverse discrete Fourier transform is $1/\Delta f$. This corresponds to the maximum range R_s given as

$$R_s = \frac{c}{2\Delta f}. \quad (16)$$

Therefore, the maximum measurable range $R_{\max}$ is given by

$$R_{\max} = \min\left(R_p, R_s\right). \quad (17)$$

III. Design and Implementation

A. Waveguide to Microstrip Coupler

In this work, we use a VNA and extension modules spanning 220–330 GHz to characterize the LWA. As the VNA suite transmits and receives signals through a WR-3 rectangular waveguide, a waveguide-to-microsrip coupler is required to connect the LWA to the VNA. For this purpose, here we develop a via-less coupler as illustrated in Fig. 1(b) that allows non-collinear mode conversion between a waveguide and a microstrip line. The coupler is based on a pair of patches located on and above the aperture of the waveguide [30]. The top patch is extended over the length of b=155 μm to define a quarter-wave stub that prevents wave leakage into free space during the mode conversion. The structure is constructed from two cyclic olefin polymer (COP) films, onto each of which a metal strip and a ground are patterned

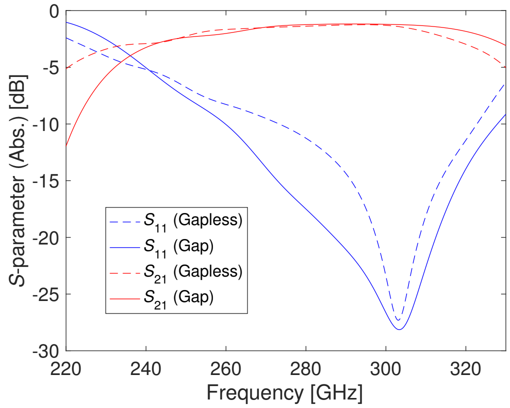

Fig. 3. Calculated S-parameters of a single coupler including a short microstrip line of 0.94 mm long as shown in Fig. 1(b). Gap denotes an airgap of 7 μm thick inserted between the two polymer films to account for fabrication tolerance.

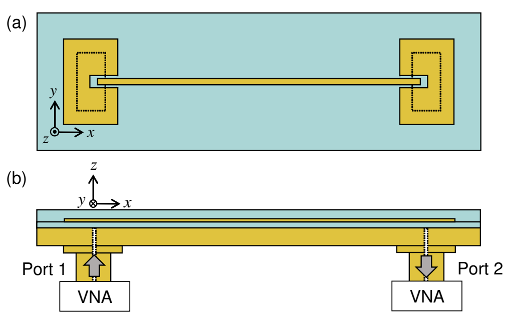

Fig. 4. Back-to-back structure consisting of two identical couplers and an unloaded microstrip line of 23 mm long for thru-reflect measurement.

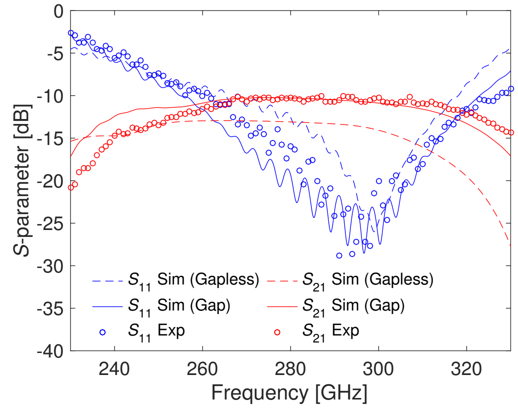

Fig. 5. Measured and calculated S-parameters of the back-to-back structure. Gap denotes an airgap of 7 μm thick inserted between the two polymer films to account for fabrication tolerance.

separately as shown in Fig. 1(b). Typically, the COP has a relative permittivity of 2.3 and is suited for developing terahertz components as it is relatively low loss and can easily be metalized [33]. In this work, we find that $\tan\delta$=0.009 used in the simulation reproduces the experimental results well, and hence we assume this value hereafter. The structural parameters are optimized with CST Microwave Studio. To calculate the S-parameters of the coupler, the microstrip line extends 0.94 mm before being terminated with a matched port. The calculated S-parameters are shown in Fig. 3 (dashed curves). The insertion loss at 300 GHz is 1.2 dB, and the 3 dB transmission bandwidth of S_{21} is beyond 95 GHz (235–330 GHz), limited by the measurable range with the current equipment. The metal patterns are processed by sputtering 150 nm thick copper followed by laser ablation. Then the two films are stacked together on top of a metal substrate. This process creates the coupler and the microstrip line with its top surface covered with COP. The metal substrate is plated with gold and incorporates two rectangular through-holes that define WR-3 waveguide flanges (0.8636 mm × 0.4318 mm) connectable to the VNA. We manage the manual alignment of the three layers in two steps by observing alignment markers under microscope: firstly between the metal substrate and the bottom film and secondly between the bottom and top films. After the alignment, we clamp the three layers with screws. We confirmed the lateral alignment precision to be better than 10 μm from the microscope observation.

To experimentally characterize the coupler and the microstrip line, we construct a symmetric back-to-back structure as illustrated in Fig. 4 and connect to a VNA (VDI WR3.4VNAX connected to Agilent PNA Network Analyzer E8361C). The measured S-parameters are shown in Fig. 5 (circles). We confirm broadband transmission with a 3 dB bandwidth of 73 GHz (251–324 GHz) for S_{21} and 68 GHz (259–327 GHz) where $S_{11} \leq -10$ dB. Although there is a slight discrepancy between the experiment and the simulation of the original design (dashed curves), we find that the introduction of an airgap of 7 μm between the two polymer films in the simulation model (solid curves) reproduces the experimental result well. This airgap models an imperfection in the layer stacking. Notably, the airgap enhances S_{21} and shifts the curve toward higher frequencies due to the reduced effective dielectric loss and permittivity of the substrate. We also recalculate the S-parameters of a single coupler including the airgap. The result is shown by the solid curves in Fig. 3. We next calculate the propagation constant of the microstrip line. Figure 6 (solid and dashed curves in red) shows the calculated propagation constant with and without the airgap. Without the air gap, the effective permittivity of the microstrip line is 2.3. This value is equal to the relative permittivity of COP because the fringing E field is fully inside the encapsulating COP layer. The air gap reduces the effective permittivity of the microstrip to 2.1. We also calculate the attenuation coefficient of the microstrip line, α_m defined in (3), as shown in Fig. 7 (solid and dashed curves in red). At 300 GHz, we obtain $\alpha_m = 0.042$ mm^{-1} (with airgap) and 0.058 mm^{-1} (without airgap). These are equivalent to 0.37 dB/mm and 0.50 dB/mm, respectively, and are comparable to or less than previously reported values (0.5 dB/mm in [34] and 0.9 dB/mm in [35]).

B. Leaky-Wave Antenna

We implement a LWA by periodically loading stubs on the microstrip line as illustrated in Fig. 1(a). As the electric field is

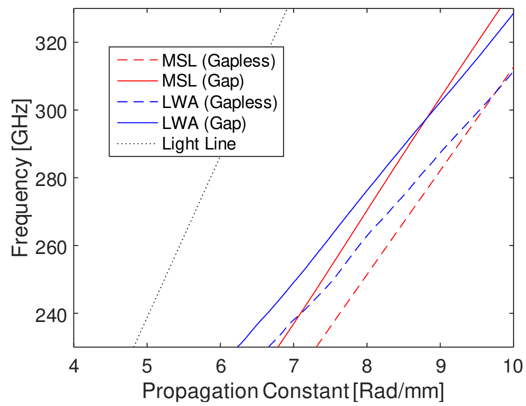

Fig. 6. Dispersion relation extracted from simulation. MSL denotes a microstrip line without radiating stubs. LWA denotes a microstrip line with the stubs. Gap denotes an airgap of 7 μm thick inserted between the two polymer films.

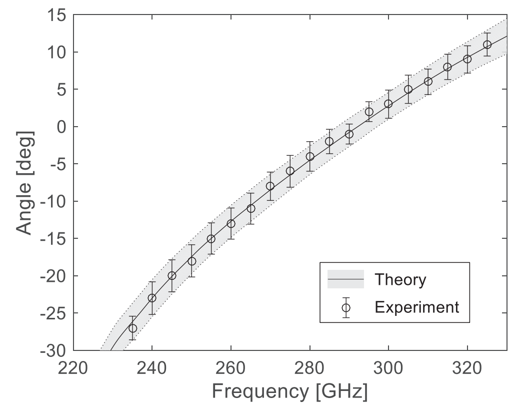

Fig. 8. Measured and calculated beam angle as a function of the frequency. The bars indicate the experimental 3 dB beam widths while the gray hatched area shows the theoretical beam width calculated by (4).

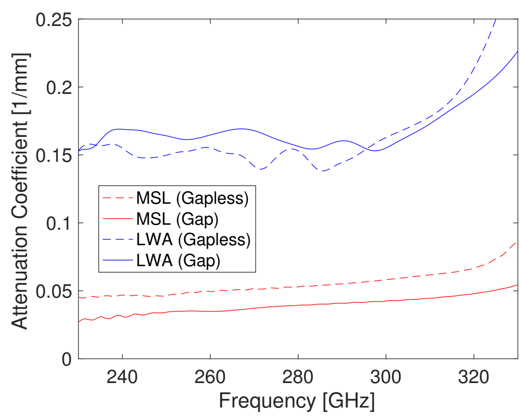

Fig. 7. Attenuation coefficients extracted from simulation. MSL denotes a microstrip line without stubs. LWA denotes a microstrip line with the stubs. Gap denotes an airgap of 7 μm thick inserted between the two polymer films.

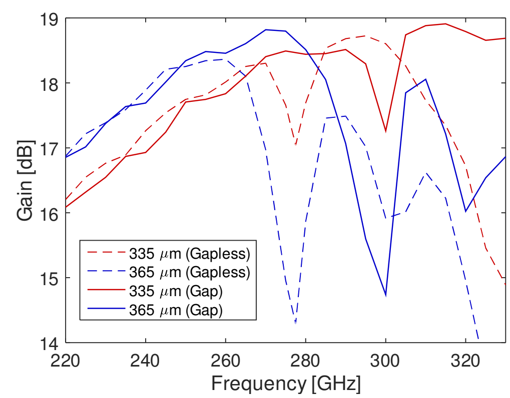

Fig. 9. Calculated antenna gain for different stub lengths.

distributed symmetrically along the line, a comb structure [36], [37] can be used to enhance the radiation efficiency and also double the aperture width in the transverse direction. Instead of the back-to-back configuration used in Sec. III-A, here we use a single coupler connected to a sufficiently long LWA consisting of 36 stub periods with a period $p = 730$ μm. To determine the beam angle and width from (1) and (4), we consider the propagation constant β_g and attenuation coefficient α of the stub-loaded microtstrip line. Although we have obtained β_g of the unloaded microstrip line as shown by the red curves in Fig. 6, the periodic stubs collectively behave as a microstrip filter and involve frequency-dependent perturbation on β_g [19]. To account for this effect, we numerically recalculate the dispersion relation with the stubs and show the result by the blue curves in Fig. 6. The stubs result in the effective permittivity of the microstrip ranging from 1.7 to 2.1 as the frequency varies from 230 GHz to 330 GHz. The theoretical beam angle is then obtained as a function of the frequency as shown by the solid curve in Fig. 8. Likewise, the periodic stubs also modulate the attenuation coefficient of the microstrip line by involving radiation losses. With the periodic stubs, the attenuation coefficient is given by the blue curves in Fig. 7. This leads to $\alpha = 0.155$ mm^{-1} (with the airgap) including the radiation loss of $\alpha_r = 0.116$ mm^{-1} at 300 GHz as defined in (3). With this value, the beamwidth estimated from (4) becomes $\theta_w \simeq 4°$, which is shown by the gray hatched area in Fig. 8. We also estimate that nearly 80% of the power excited on the LWA is radiated into free-space while the remaining 20% is dissipated by the metallic and dielectric losses. The power remaining on the microstrip line after passing through all the stubs becomes less than -40 dB across the operation bandwidth. This power level is sufficiently low so that no additional termination is required.

Although periodic LWAs generally suffer an open stopband issue, where the broadside radiation is significantly suppressed due to the Bragg reflection, it has recently been discussed that the optimization of the array geometry can mitigate or negate the stopband [19]–[22]. Here we numerically investigate the influence of the stub length on the open stopband. Figure 9 shows the antenna gain for two different stub lengths. While the gain shows significant drop when the stub length $l = 365$ μm (=0.5p) (blue curves) as in conventional designs [36], [37], we find this drop can be significantly mitigated by tuning the stub length. Based on parametric optimization, we

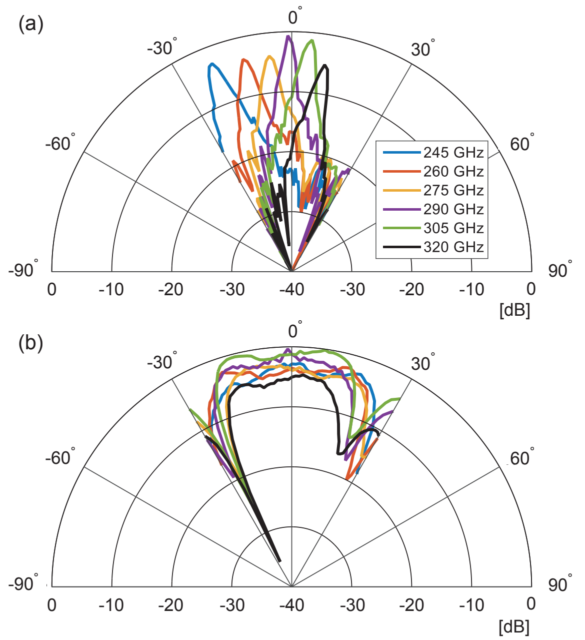

Fig. 10. Examples of the measured beam patterns in (a) H-plane and (b) E-plane. (b) shares the same notation as (a). The H-plane corresponds to the xz-plane defined in Fig. 1. The E- plane is aligned with the main lobe direction at each frequency.

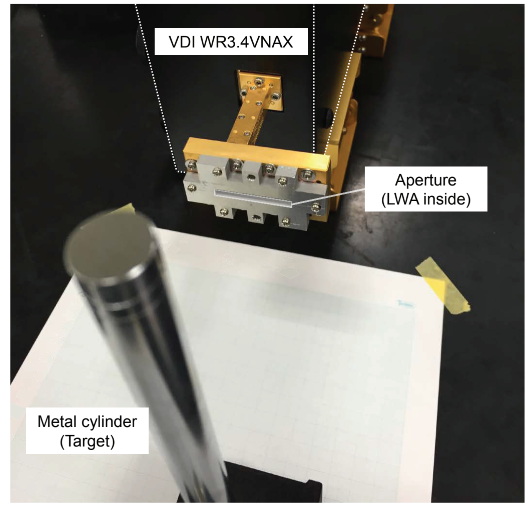

Fig. 11. Photograph of experimental setup, which is schematically illustrated in Fig. 1(a).

choose $l = 335$ μm (=0.46p) (red curves) in our design. We also confirm that the existence of the airgap does not affect this mitigation except for shifting the frequency (solid vs dashed curves).

We experimentally characterize the radiation pattern of the LWA inside an anechoic chamber using another set of VNA extenders (OML V03VNA2). We attach the LWA on port 1 and a standard horn antenna on port 2. Port 1 is mounted on an automated stage that can rotate around 2-axes while port 2 is fixed. The distance from the LWA to the receiving horn is set to nearly 32 cm. The beam pattern is measured by recording S_{21} while rotating the LWA. The rotation range is limited to $\pm 30°$ in both axes. Figures 10(a, b) show examples of the measured beam patterns in the H-plane and E-plane, respectively. The H-plane corresponds to the xz-plane as illustrated in Fig. 1(a). We clearly observe a directional beam steerable in the H-plane by sweeping the frequency. On the other hand, it spreads broadly in the transversal E-plane and is insensitive to the frequency. The experimental beam angle in the H-plane is summarized in Fig. 8 (circles). The beam is steerable from $-23°$ to +15° when sweeping the frequency from 235 to 325 GHz. The experimental result (circles) agrees well with the analytical result (solid curve). The accompanying bars indicating the observed 3 dB beam widths also agree with the analytical result (gray hatched area). Although the frequency sweep range is limited by the used VNA extenders, steering over a wider range will be possible by extending the frequency. While no higher order diffraction is allowed for lower frequencies, the second order diffraction is expected to appear above 330 GHz.

IV. Application to Short Range Radar

Using the LWA developed in Sec. III-B, we experimentally demonstrate short-range terahertz radar for small target detection. As a test target, we place a metal cylinder with a diameter of 12 mm in front of the LWA as shown in Fig. 11. The cylinder has a length of 176 mm in the y-direction. We extract its location by measuring S_{11} of the LWA. It should be mentioned that the experiment in this section is performed on a tabletop outside the chamber to freely and accurately translate the target. Therefore, time-invariant scattering from the background becomes a noise source. By assuming the VNA's dynamic range of 100 dB $\left(|\Gamma_{\min}| = 10^{-5}\right)$, the LWA's gain of 18 dB $\left(G = 10^{1.8}\right)$, and the projected cross section of the metal cylinder $\sigma = 0.002\ \mathrm{m}^2$, the maximum measurable range limited by the radar equation is $R_p = 2.5$ m from (15). Suppose the dynamic range is decreased to 60 dB due to the background noise, R_p reduces to 25 cm. Meanwhile, since we set the sampling interval of the VNA as $\Delta f = 1.0$ GHz for experimental convenience, the measurable range limited by the sampling interval is $R_s = 15$ cm from (16). In this case, the measurable range is governed by the sampling interval. The sampling interval can be decreased at the expense of the measurement time.

Keeping this limitation in mind, we manually position the target in the xz-plane. Figure 12 presents examples of the detected reflection coefficients in the frequency- and time-domains when the target location (x, z) is (a,b) (0 mm, 46 mm), (c,d) (0 mm, 66 mm), and (e,f) (10 mm, 66 mm). The top row (a,c,e) shows frequency-domain results extracted by using (6), and the bottom row (b,d,f) shows time-domain results calculated from their inverse Fourier transform. We observe well-defined peaks in all the graphs. By comparing (a,b) and (c,d), we see that the target translation in the z-direction at constant x involves a peak shift in the time-domain. On the other hand, by comparing (c,d) and (e,f), the translation in the x-direction at constant z involves a

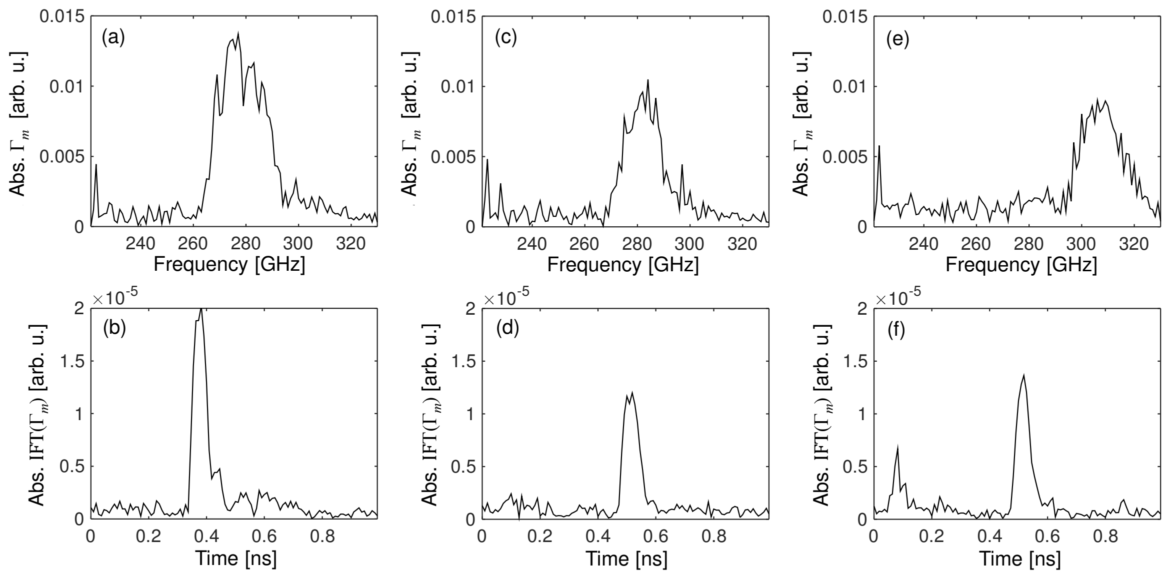

Fig. 12. Examples of the detected reflection coefficients. The top row (a,c,e) shows frequency-domain results, and the bottom row (b,d,f) shows time-domain results. The target locations (x, z) are (a,b) (0 mm, 46 mm), (c,d) (0 mm, 66 mm), and (e,f) (10 mm, 66 mm).

peak shift in the frequency-domain. The peak positions in the frequency- and time-domain can be respectively translated into the direction θ_t and range R_t of the target by (9) and (10). The extracted target locations are plotted in the Cartesian coordinate in Fig. 13, where the target is translated along the x-direction at different z positions. The extracted centers (*) show agreement with the true centers (+) with a mean error of 2.5 mm. The position errors might be attributed to the background noise, the manual alignment of the target, the slight deflection of the cylinder, and a drift of the VNA calibration. The dashed circles correspond to the uncertainty of the direction and range defined by the 3 dB width, while the dotted circles indicate the actual outline of the cylinder. Figure 14 summarizes the corresponding direction and range. The average 3 dB widths are (a) 4.2°, (c) 3.7°, (e) 2.3° and (b) 6.2 mm, (d) 6.9 mm, (f) 7.4 mm, respectively, where we observe the trade-off in the uncertainties between the direction and range as expected. Although the 3 dB criterion provides an intuitive measure of the uncertainty, it is too tight to use as a threshold between zero and non-zero components in (11). Therefore, we roughly estimate the 10 dB width of all the peaks and obtain $N_f \cdot N_\tau \simeq 238$ on average, which is larger than the total sample points N=110 as stated by (11). The result demonstrates accurate and high-resolution terahertz radar.

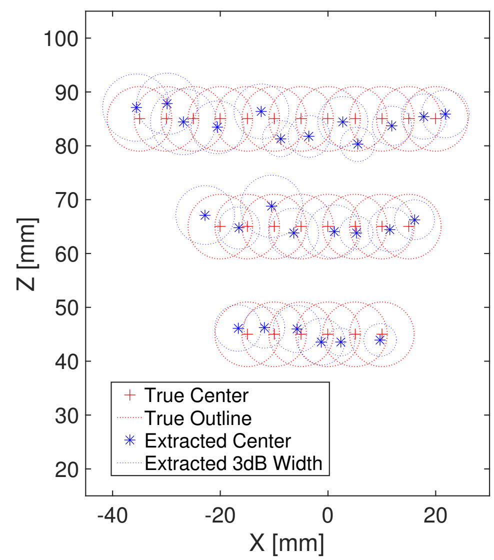

Fig. 13. 2D map of the extracted target positions. The actual center point and the outline of the cylinder are indicated by (+) and red dotted circles, respectively. The extracted target positions and the 3 dB uncertainty are presented by (*) and blue dotted circles.

V. Conclusion

In conclusion, we have proposed and demonstrated short-range terahertz radar using a LWA. We have discussed the procedure of extracting the target location by measuring the reflection coefficients of a LWA. For experimental demonstration, we have developed a microstrip periodic LWA and also a waveguide-to-microstrip coupler that interfaces the LWA and VNA. The coupler has an insertion loss of 1.2 dB at 300 GHz and the 3 dB transmission bandwidth beyond 95 GHz. By driving the LWA with a VNA, we have demonstrated beam steering from $-23°$ to $+15°$ by sweeping the frequency from 235 to 325 GHz with a nearly constant beam width of 4° across the bandwidth. Using the LWA, we have demonstrated detection and ranging of a metal cylinder with a diameter of 12 mm. We have identified the location with a mean error of 2.4 mm when the object is placed at 46, 66, and 86 mm in front of the LWA. The result demonstrates accurate and

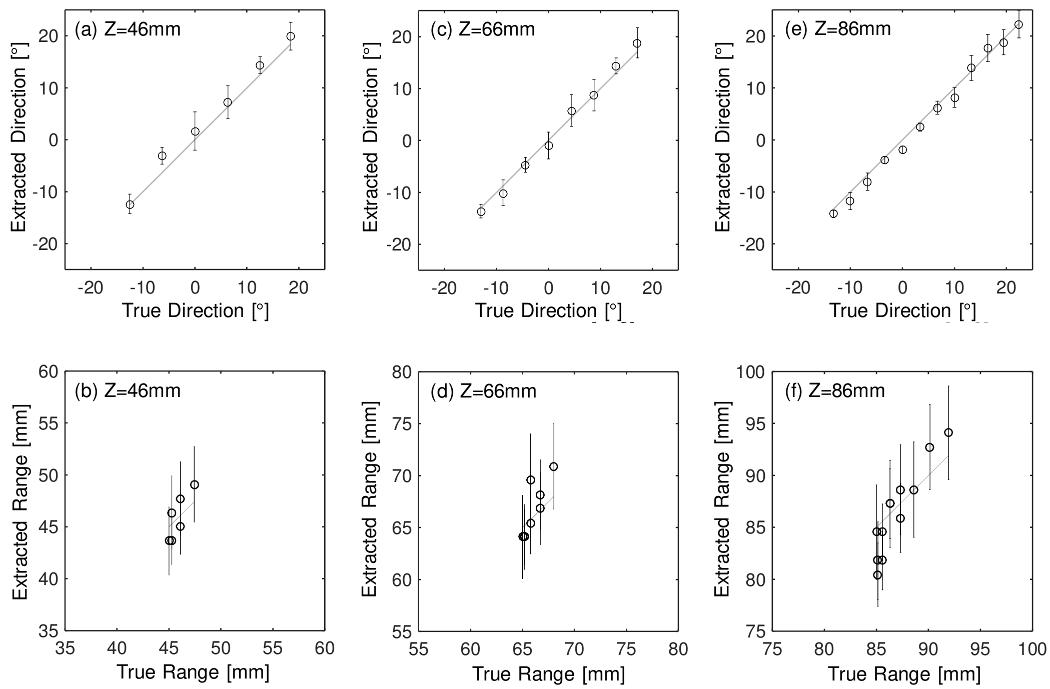

Fig. 14. Extracted direction (a,c,e) and range (b,d,f) of the target when it is translated along the x-direction at a constant z position of (a,b) 46 mm, (c,d) 66 mm, and (e,f) 86 mm. The error bars indicate the 3 dB width of the peak of the reflection coefficients in the frequency- and time-domains.

high-resolution terahertz radar.

While we have dealt with single target detection in this article, the extension to multi-target detection will be possible by carefully analyzing reflection coefficients accommodating multi peaks or more complicated spectra. To extend the measurable range of the radar, increasing the gain of the LWA is important. For this purpose, the use of lower loss materials such as cyclic olefin copolymer (COC) [38], [39] is promising. Extending the LWA aperture into 2D will also greatly increases the antenna gain, but this requires the development of 2D beam steering.

The use of a LWA can remove bulky spatial optics and pave a way for developing integrated terahertz radar incorporating solid-state sources and detectors. This integrated radar platform is particularly promising for novel applications such as flight support of tiny drones or human gesture recognition on wearable devices, both requiring high-resolution and high-speed detection with a small system footprint.

Acknowledgment

This work was supported by the Strategic Information and Communications R&D Promotion Programme (SCOPE) #165103002 from the Ministry of Internal Affairs and Communications and by the Scientific Grants-in-Aid from the Ministry of Education, Culture, Sports, Science and Technology, Japan. W. Withayachumnankul acknowledges the International Research Fellowship from the Japan Society for the Promotion of Science (JSPS).

References

[1] R. Piesiewicz, T. Kleine-Ostmann, N. Krumbholz, D. Mittleman, M. Koch, J. Schoebel, and T. Kuerner, "Short-range ultra-broadband terahertz communications: concepts and perspectives," *IEEE Antenna. Propag. Mag.*, vol. 49, pp. 24-39, Dec. 2007.

[2] K. B. Cooper, R. J. Dengler, N. Llombart, T. Bryllert, G. Chattopadhyay, E. Schlecht, J. Gill et al., "Penetrating 3D imaging at 4 and 25m range using a submillimeterwave radar," *IEEE Trans. Microwav. Theory. Tech.*, vol. 56, no. 12, pp. 2771-2778, Dec. 2008.

[3] N. Llombart, K. B. Cooper, R. J. Dengler, T. Bryllert, G. Chattopadhyay, and P. H. Siegel, "Timedelay multiplexing of two beams in a terahertz imaging radar," *IEEE Trans. Microwav. Theory. Tech.*, vol. 58, no. 7, pp. 1999-2007, Jul. 2010.

[4] Y. W. Huang, T. F. Tseng, C. C. Kuo, Y. J. Hwang, and C. K. Sun. "Fiberbased sweptsource terahertz radar." *Opt. Lett.*, vol. 35, no. 9, pp. 1344-1346, May 2010.

[5] K. Iwaszczuk, H. Heiselberg, and P. U. Jepsen, "Terahertz radar cross section measurements," *Opt. Exp.*, vol. 18, no. 25, pp. 26399-26408, Dec. 2010.

[6] K. B. Cooper, R. J. Dengler, N. Llombart, B. Thomas, G. Chattopadhyay, and P. H. Siegel, "THz imaging radar for standoff personnel screening", *IEEE Trans. Terahertz Sci. Technol.*, vol. 1, no. 1, Sep. 2011.

[7] R. Gente, C. Jansen, R. Geise, O. Peters, M. Gente, N. Krumbholz, C. Moller, S. Busch, and M. Koch, "Scaled bistatic radar cross section measurements of aircraft with a fiber-coupled THz time-domain spectrometer," *IEEE Trans. Terahertz Sci. Technol.*, vol. 2, no. 4, pp. 424-431, May. 2012.

[8] R. C. Johnson, *Antenna Engineering Handbook*, McGraw-Hill, 1993.

[9] C. A. Balanis, *Modern Antenna Handbook*, Wiley, 2008.

[10] D. R. Jackson, C. Caloz, and T. Itoh, "Leaky-wave antennas," *Proc. IEEE*, vol. 100, no. 7, pp. 2194-2206, Jul. 2012.

[11] A. Basu and T. Itoh, "Dielectric waveguide-based leaky-wave antenna at 212 GHz," *IEEE Trans. Antenna. Propag.*, vol. 46, no. 11, pp. 1665-1673, Nov. 1998.

[12] Y. Monnai, K. Altmann, C. Jansen, M. Koch, H. Hillmer, and H. Shinoda, "Terahertz beam focusing based on plasmonic waveguide scattering," *Appl. Phys. Lett.*, vol.101, no.15, 15116, Oct. 2012.

[13] Y. Monnai, D. Jahn, W. Withayachumnankul, M. Koch, and H. Shinoda "Terahertz plasmonic bessel beamformer," *Appl. Phys. Lett.*, vol.106, no.2, 021101, Jan. 2015.

[14] N. J. Karl, R. McKinney, Y. Monnai, R. Mendis, and D. Mittleman, "Frequency-domain multiplexing in the terahertz range using a leaky wave antenna," *Nature Photon.*, vol.9, 717, Sep. 2015.

[15] R. McKinney, Y. Monnai, R. Mendis, and D. Mittleman, "Focused

terahertz waves generated by a phase velocity gradient in a parallel-plate waveguide," *Opt. Exp.*, vol.23, no.21, 27947, Oct. 2015.
[16] P. W. C. Hon, Z. Liu, T. Itoh, and B.S. Williams, "Leaky and bound modes in terahertz metasurfaces made of transmission-line metamaterials," *J. Appl. Phys.*, vol. 113, pp. 033105, Jan. 2013.
[17] M. Esquius-Morote, J.S. Gomez-Diaz, and J. Perruisseau-Carrier, "Sinusoidally modulated graphene leaky-wave antenna for electronic beam scanning at THz," *IEEE Trans. Terahertz Sci. Technol.*, vol. 4, no. 1, pp. 116122, Jan. 2014.
[18] A. A. Tavallaee, B. S. Williams, P. W. Hon, T. Itoh, and Q. S. Chen, "Terahertz quantum-cascade laser with active leaky-wave antenna," *Appl. Phys. Lett.*, vol. 99, no. 14, 141115, Oct. 2011.
[19] P. Baccarelli, S. Paulotto, D. R. Jackson, and A. A. Oliner, "A new Brillouin dispersion diagram for 1-D periodic printed structures," *IEEE Trans. Microwave Theory. Tech.*, vol. 55, no.7, pp. 1484-1495, Jul. 2007.
[20] S. Paulotto, P. Baccarelli, F. Frezza, and D. R. Jackson, "A novel technique for open-stopband suppression in 1-D periodic printed leaky-wave antennas," *IEEE Trans. Antenna. Propag.* vol. 57, no. 7, pp. 1894-1906, Jul. 2009.
[21] S. Otto, A. Rennings, K. Solbach, C. Caloz, "Transmission line modeling and asymptotic formulas for periodic leaky-wave antennas scanning through broadside," *IEEE Trans. Antennas. Propag.*, vol. 59, no. 10, pp. 3695-3709, Aug. 2011.
[22] J. T. Williams, P. Baccarelli, S. Paulotto, and D. R. Jackson, "1-D combline leaky-wave antenna with the open-stopband suppressed: Design considerations and comparisons with measurements," *IEEE Trans. Antenna. Propag.*, vol. 61, no. 9, pp. 4484-4492, Jun. 2013.
[23] T. Maekawa, H. Kanaya, S. Suzuki, and M. Asada, "Oscillation up to 1.92 THz in resonant tunneling diode by reduced conduction loss," *Appl. Phys. Exp.*, vol. 9, no. 2, 024101, Jan. 2016.
[24] S. Kitagawa, S. Suzuki, and M. Asada, "650-GHz resonant-tunneling-diode VCO with wide tuning range" *IEEE Electron Dev. Lett.*, vol. 35, no. 12, pp. 1215-1217, Dec. 2014.
[25] B. J. Williams, "Terahertz quantum-cascade lasers," *Nature Photon.*, vol. 1, pp. 517-525, Sep. 2007.
[26] A. Rogalski and F. Sizov, "Terahertz detectors and focal plane arrays," *Opt-Electron. Rev.*, vol. 19, no. 3, Sep. 2011.
[27] B. M. Albaker and N. A. Rahim, "Unmanned aircraft collision detection and resolution: concept and survey," *Proc. IEEE Conf. Industrial Electron. Apps.*, 2010.
[28] Google Project Soli, https://www.google.com/atap/project-soli/, 2015.
[29] H. E. Bass, L. C. Sutherland, A. J. Zuckerwar, D. T. Blackstock, and D. M. Hester, "Atmospheric absorption of sound: Further developments," *J. Acoust. Soc. Am.*, vol. 97, no. 1, pp. 680- 683, Jan. 1995.
[30] K. Seo, A. Nakatsu, K. Sakakibara, and N. Kikuma, "Via-hole-less planar microstrip-to-waveguide transition in millimeter-wave band," *Proc. China-Japan Joint Microwave Conference*, 2011, pp.1-4.
[31] D. M. Pozar, *Microwave Engineering*, 4th ed., Wiley, 2011.
[32] D. L. Donoho and P. B. Stark, "Uncertainty principles and signal recovery," *SIAM J. Appl. Math.*, vol. 49, no. 3, pp. 906931, Jun. 1989.
[33] Y. Kishi, M. Nagai, J. C. Young, K. Takano, M. Hangyo, and T. Suzuki, "Terahertz laminated-structure polarizer with high extinction ratio and transmission power," *Appl. Phys. Exp.*, vol. 8, no. 3, 032201, Feb. 2015.
[34] T. Tajima, H. J. Song, and M. Yaita, "300-GHz microstrip-to-waveguide transition on a polyimide substrate integrated with an LTCC substrate integrated waveguide," *IEICE Trans.*, vol. E-98-C, no. 12, pp. 1120-1127, Dec. 2015.
[35] S. Keya, A. Ghaddar, T. Akalin, M. Chudzik, I. Arnedo, I. Arregui, F. Teberio, A. Lujambio, T. Lopetegi, "Low loss transitions and microstrip lines on cyclo-olefin co-polymer substrate for terahertz applications," *Proc. MMS*, 2013, pp. 1-3.
[36] J. R. James and P. S. Hall, "Microstrip antennas and arrays. Part 2 New array-design technique," *IEE J. Microwav. Opt. Acoust.*, vol. 1, no. 5, pp. 175-181, Sep. 1977.
[37] J. R. James, P. Hall, and C. Wood, *Microstrip Antenna Theory and Design*, Peter Perefrinus Ltd., 1981.
[38] A. Sengupta, A. Bandyopadhyay, B. F. Bowden, J. A. Harrington, and J. F. Federici, "Characterisation of olefin copolymers using terahertz spectroscopy," *Electron. Lett.*, vol. 42, no. 25, Dec. 2006.
[39] E. Peytavit, C. Donche, S. Lepilliet, G. Ducournau and J.F. Lampin, "Thin-film transmission lines using cyclic olefin copolymer for millimetre-wave and terahertz integrated circuits," *Electron Lett.*, vol. 47, no. 7, pp. 453-454, Mar. 2011.

Kosuke Murano Kosuke Murano was born in Kanagawa, Japan on Mar. 11, 1994. He received the B.S. degree in Applied Physics and Physico-Informatics from Keio University, Japan, in 2016. Currently, he is pursuing the M.S. degree at Keio University. Since 2015, he has engaged in a research on the terahertz radar based on leaky-wave antenna. His research interests include terahertz solid-state sources and detectors.

Issei Watanabe Issei Watanabe received the B.E., M.E. and Ph.D. degrees in engineering science from Osaka University in 1999, 2001 and 2005, respectively. From 2001 to 2004, he joined collaboration team among Osaka University, Communications Research Laboratory (CRL) and Fujitsu Laboratories Limited, where he worked on growth of epitaxial heterostructure by MBE and fabrication and characterization of cryogenically cooled InP-based InGaAs/InAlAs HEMTs. In 2004, he joined the National Institute of Information and Communications Technology (NICT, formerly CRL), Tokyo, Japan, where he has been engaged in the research and development of nanoscale gate compound semiconductor electron devices and circuits, and high-frequency measurement technology for millimeter- and THz-wave applications.

Dr. Watanabe is a member of the Japan Society of Applied Physics (JSAP) and the Institute of Electronics, Information and Communication Engineers (IEICE).

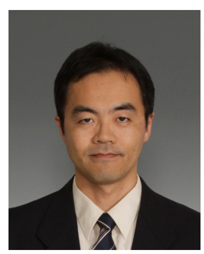

Akifumi Kasamatsu Akifumi Kasamatsu received his B.E. and M.E. and Ph.D. degrees in electronics engineering from Sophia University, Tokyo, Japan, in 1991, 1993 and 1997, respectively. From 1997 to 1999, he was a research assistant at Sophia University. From 1999 to 2002, he was with Fujitsu Laboratories Ltd., Atsugi, Japan. Since 2002, he has joined National Institute of Information and Communications Technology (NICT), Koganei, Japan, where he is currently working as an excecutive resarcher and a principal investigator of the terahertz wave electronics project. His current research interests are in wireless communication technology such as wireless transceivers and nano-scale semiconductor devices for millimeter wave and terahertz wave communications.

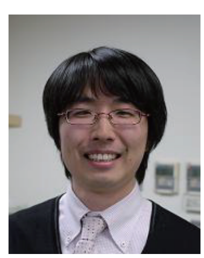

Safumi Suzuki Safumi Suzuki received the B.E. degree in Electrical and Electronic Engineering and the M.E. and D.E. degrees in Electronics and Applied Physics from the Tokyo Institute of Technology, Japan, in 2005, 2007, and 2009, respectively. From 2009 to 2014, he was an Assistant Professor in the Department of Electronics and Applied Physics, Tokyo Institute of Technology, and was an Associate Professor in the Department of Physical Electronics from 2014 to 2016. He has been an Associate Professor in the Department of Electrical and Electronic Engineering since 2016. He is currently engaged in research on THz electron devices.

Dr. Suzuki is a member of the Japan Society of Applied Physics (JSAP) and the Institute of Electronics, Information and Communication Engineers (IEICE) of Japan.

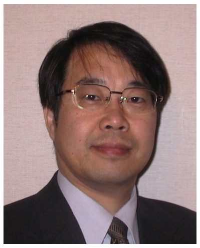

Masahiro Asada Masahiro Asada (F'12) received the B.E., M.E., and D.E. degrees in Physical Electronics from the Tokyo Institute of Technology, Japan, in 1979, 1981, and 1984, respectively. In 1984, he joined the Department of Physical Electronics, Tokyo Institute of Technology as a Research Associate. From 1986 to 1987, he was with the Physics Institute of Stuttgart University, Stuttgart, Germany, as a Research Fellow of the Alexander von Humboldt Foundation. From 1988 to 1999, he was an Associate Professor in the Department of Electrical and Electronic Engineering, Tokyo Institute of Technology and was a Professor in the Interdisciplinary Graduate School of Science and Engineering from 1999-2016. He is currently a Professor in the Institute of Innovative Research, Tokyo Institute of Technology. His current research is on high-frequency electron devices, especially THz devices using nanostructures.

Withawat Withayachumnankul Withawat Withayachumnankul received the B.Eng. and M.Eng degrees in electronic engineering from King Mongkut's Institute of Technology Ladkrabang (KMITL), Bangkok, Thailand, in 2001 and 2003, respectively, and the Ph.D. degree in electrical engineering (with commendation) from the University of Adelaide, Adelaide, Australia, in 2010. From 2003-2012, he served as a Lecturer at KMITL with the Faculty of Engineering. From 2010-2013, he has held an ARC Australian Postdoctoral Fellowship with the University of Adelaide, and has become a Lecturer there in 2014. In 2015, he was an International Research Fellow of the Japan Society for the Promotion of Science (JSPS) at Tokyo Institute of Technology. Since 2012, he has been appointed as an Associate of RMIT University, Melbourne, Australia. His research interests include terahertz technology, metamaterials, plasmonics, and optical antennas.

Toshiyuki Tanaka Toshiyuki Tanaka received B.E., M.E. and Dr. Eng. degrees in Instrumentation Engineering, from Keio University, Yokohama, Japan, in 1982, 1984 and 1989, respectively. In 1989, he joined Department of Instrumentation Engineering, Faculty of Science and Technology, Keio University as a Research Assistant. He was an Assistant Professor in Instrumentation Engineering from 1993-1996, an Assistant Professor in Department of Applied Physics and Physico-Informatics from 1996-2003, an Associate Professor from 2003-2009. He is currently a Professor in Applied Physics and Physico-Informatics, Keio University. His research interests are in image processing of medical applications, biometric authentication, non-destructive inspection, GPS, nonlinear problems, and THz devices.

Yasuaki Monnai Yasuaki Monnai received his B.E. degree in Mathematical Engineering and Information Physics and M.S. and Ph.D. degree in Information Physics and Computing from the University of Tokyo, Japan, in 2008, 2010, and 2013, respectively. From 2010 to 2013, he served as a Research Fellow of Japan Society for the Promotion of Science. From 2010 to 2011, he was a Visiting Scholar with the University of Kassel, and in 2012 with Philipps University of Marburg, both in Germany. From 2013 to 2015, he served as a Project Assistant Professor with the University of Toyko. Since 2015, he became an Assitant Professor with the Deparment of Applied Physics and Physico-Informatics, Keio University, Japan. His research interest includes exploring wireless systems for interfacing humans, machines, and materials. Technical areas of interest include, but are not limited to, microwaves, terahertz waves, and ultrasound.